Journal of Power Sources 186 (2009) 185–193

Contents lists available at ScienceDirect

Journal of Power Sources

journal homepage: www.elsevier.com/locate/jpowsour

Hydrogen storage properties of Mg_xFe (x: 2, 3 and 15) compounds produced by reactive ball milling

J.A. Puszkiel*, P. Arneodo Larochette, F.C. Gennari

Instituto Balseiro (UNCuyo and CNEA), Consejo Nacional de Investigaciones Científicas y Técnicas (CONICET) and Centro Atómico Bariloche, Av. Bustillo km 9.5, R8402AGP, S.C. de Bariloche, Argentina

ARTICLE INFO

Article history:
Received 1 August 2008
Received in revised form
23 September 2008
Accepted 24 September 2008
Available online 7 October 2008

Keywords:
Hydrogen storage
Reactive ball milling
Metal hydrides

ABSTRACT

This work deals with the assessment of the thermo-kinetic properties of Mg–Fe based materials for hydrogen storage. Samples are prepared from Mg_xFe (x: 2, 3 and 15) elemental powder mixtures via low energy ball milling under hydrogen atmosphere at room temperature. The highest yield is obtained with $Mg_{15}Fe$ after 150 h of milling (90 wt% of MgH_2). The thermodynamic characterization carried out between 523 and 673 K shows that the obtained Mg–Fe–H hydride systems have similar thermodynamic parameters, i.e. enthalpy and entropy. However, in equilibrium conditions, $Mg_{15}Fe$ has higher hydrogen capacity and small hysteresis. In dynamic conditions, $Mg_{15}Fe$ also shows better hydrogen capacity (4.85 wt% at 623 K absorbed in less than 10 min and after 100 absorption/desorption cycles), reasonably good absorption/desorption times and cycling stability in comparison to the other studied compositions. From hydrogen uptake rate measurements performed at 573 and 623 K, the rate-limiting step of the hydrogen uptake reaction is determined by fitting particle kinetic models. According to our results, the hydrogen uptake is diffusion controlled, and this mechanism does not change with the Mg–Fe proportion and temperature.

1. Introduction

In recent years the demand for an alternative energy carrier for vehicular applications has become more pronounced due to the increasing price of oil-derived fuels and the pollutant emissions that their burning produces (CO_2, NO_x). Hydrogen is one of the most attractive alternatives owing to its abundance, easy synthesis and non-polluting nature when used in fuel cells. Nevertheless, for its commercial application one of the technological constraints that must be tackled is the storage of this highly inflammable gas in an efficient and safe way. The relatively advanced method such as high-pressure gas and liquefied hydrogen tanks cannot fulfill the established storage goals (6 wt% H and 45 kg L^{-1} for 2010) [1], since they are neither safe nor density-efficient storage procedures (hydrogen gas: 0.99×10^{22} H atoms cm^{-3}; liquefied hydrogen: 4.2×10^{22} H atoms cm^{-3}). Solid-state storage of hydrogen in metal hydride form gives a safety advantage over the gas and liquid storage methods. In addition, metal hydrides have higher hydrogen storage density (6.5×10^{22} H atoms cm^{-3} for MgH_2) [2].

Magnesium hydride is considered as a potential candidate for solid-state hydrogen storage for on-board applications. MgH_2 has the highest energy density (9 MJ kg^{-1} Mg) of all reversible hydrides applicable for hydrogen storage. It also combines a high hydrogen capacity of 7.6 wt%, low cost and reversibility. Furthermore, it is abundantly available. However, the practical use of MgH_2 is precluded by the poor rates of its hydrogen release/uptake reactions, especially at temperatures below 573 K. This fact is ascribed to the strong ionic bond between Mg and H, which makes MgH_2 thermodynamically very stable within the practical useful temperature range [3].

Many efforts have been devoted to improve the hydrogen storage properties of magnesium, such as the production of micro/nanocrystalline powder and creation of defects by ball milling [4–9], synthesizing composite of metal hydrides [10–13] and adding catalyst [4,10,14–31]. Ball milling is a well-known method for processing metallic powders which can reduce the crystallite size down to the nanometer range and disperse an added catalyst effectively. Reactive ball milling (RBM) in hydrogen atmosphere is a one step synthesis method which involves the in situ synthesis of hydrides phases facilitated by the accompanied refinement of the microstructure of the materials during the process. In the case of magnesium, the crystallite size reduction and the proper dispersion of a 3d-transition metal can significantly improve the H

* Corresponding author. Tel.: +54 2944 44 5197/18; fax: +54 2944 44 5190.
E-mail address: jpuszkiel@cab.cnea.gov.ar (J.A. Puszkiel).

0378-7753/$ – see front matter © 2008 Elsevier B.V. All rights reserved.
doi:10.1016/j.jpowsour.2008.09.101

transport properties and hydrogenation–dehydrogenation kinetics [9,14,21,25,31].

One of the 3d-transition elements added to Mg in order to improve its hydrogen storage properties is Fe. The interest in the Mg–Fe–H system is based on its better hydrogen storage properties compared to the Mg–H hydride system. The former system has lower dissociation temperature and pressure than the latter system and reasonably good capacity, 5.47 wt% [32]. Despite the fact that Mg–Fe–H is considered a promising material for hydrogen storage, many of its features, like hydrogen capacity, thermodynamic stability and thermal conductivity, must be enhanced.

In order to improve the hydrogen storage properties of the Mg–Fe–H system, in the present work Mg_xFe (x: 2, 3 and 15) are investigated. Such materials are synthesized via RBM in hydrogen atmosphere at room temperature. Thermodynamics of the as-milled materials is assessed in the temperature range of 523–673 K by pressure–composition isotherm (PCI) plots (reversibility and equilibrium pressure) and van't Hoff graphs (heat of hydrogen absorption/desorption). The effects of the pressure and temperature on the kinetic behavior of the Mg–Fe–H system are evaluated. The kinetic behavior is studied between 523 and 673 K, comparing the hydrogen uptake capacity, absorption/desorption rates and cycling stability of the synthesized Mg–Fe compositions. At 573 and 623 K, typical kinetic models are applied to determine the rate-limiting step of the hydrogen absorption reaction. Throughout this study we conclude that the material with $Mg_{15}Fe$ composition has better hydrogen storage properties.

2. Experimental

2.1. Preparation of the Mg–Fe–H hydride system

The synthesis of the Mg–Fe–H system was performed via low energy ball milling in hydrogen atmosphere, i.e. RBM. Stoichiometric Mg_xFe (x: 2, 3 and 15) elemental powder mixtures (purity of the starting materials higher than 99%) were mechanically milled in a magneto-mill Uni-Ball-Mill II (Australian Scientific Instruments) device, using stainless steel balls as a grinding medium. The milling details are in Table 1.

The vial was opened several times during the milling processes in order to take samples of the as-milled powders. Before and after subtracting the samples the vial was evacuated and purged several times with argon gas (+99.9995%). During the RBM procedures the vial was refilled with hydrogen each 10 h to maintain hydrogen gas pressure of 0.5 MPa. All handling was carried out in a globe box with argon gas and oxygen and moisture controlled atmosphere, so as to minimize the oxidation of the samples.

2.2. Characterization

The microstructural and hydrogen storage properties of the samples extracted during the milling processes and the obtained hydride systems were characterized via diverse techniques. X-ray diffraction (XRD) analysis on a Philips PW 1710/01 Instruments with CuKα radiation (λ = 1.5405 Å, graphite monochromator, 30 mA and 40 kV) was employed to observe the present phases in the samples and to determine the crystallite size. The X-ray intensity was measured over diffraction angle 2θ from 10° to 90° with a scanning rate of $0.02^\circ\ s^{-1}$. Considering the crystallite size as the unique component responsible for the XRD peak broadening, the degree of microstructural refinement of MgH_2 and unreacted Fe of the as-milled powders was estimated applying the Scherrer equation. The microstructural morphology of the samples was studied by scanning electron microscopy (SEM 515, Philips Electronic Instruments) on stick dispersed powders, and resin-mounted and polished samples. The thermal behavior was investigated by differential scanning calorimetry (DSC) using a TA 2910 calorimeter at a heating rate of $5\ K\ min^{-1}$ and an argon flow rate of $122\ ml\ min^{-1}$. The amount of absorbed hydrogen and the proportion of hydride phases were estimated from the DSC curves, using the peak area and the heats of formation reported in this work.

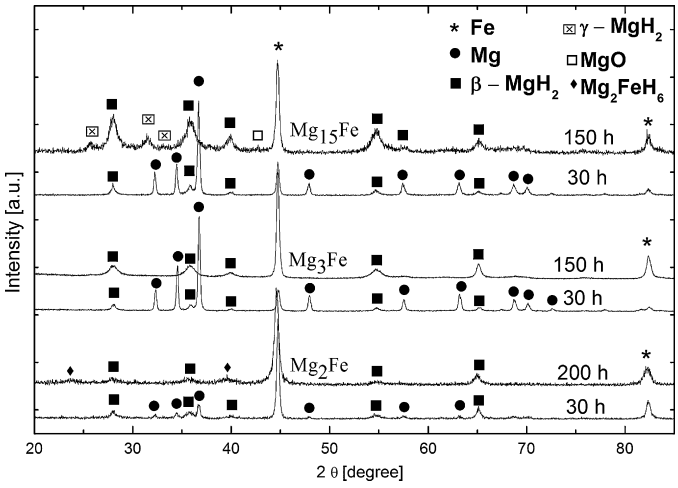

Fig. 1. X-ray diffraction patterns: Mg_2Fe, Mg_3Fe and $Mg_{15}Fe$ at 30 h and after the RBM process.

A modified Sieverts-type device coupled with a mass flow controller was used to perform both the thermodynamic and kinetic characterization [33]. Absorption/desorption PCIs were measured in the temperature range of 523–623 K in order to study the thermodynamics of the Mg–Fe–H systems. The equilibrium plateau pressures were calculated as an average of the experimental points in the plateau region, taking into account the error propagation theory to assign an error range to each calculated equilibrium pressure. From the calculated equilibrium pressures the absorption/desorption van't Hoff graphs were plotted.

Hydrogen absorption/desorption rate measurements were carried out between 573 and 623 K in the Sieverts-type device. In order to compare the temperature effects on the hydrogen uptake rates and capacities of $Mg_{15}Fe$, Mg_3Fe and Mg_2Fe, all measurements were performed at the same relationship between the initial pressure at which the absorption process starts and the respective equilibrium pressure ($P_i/P_{equilibrium} = 2.4$). This ensures that the absorption kinetics is not influenced either by different pressure drops at the tested temperatures or by the equilibrium pressure of the hydride system. Due to the experimental fluctuations, each hydrogen absorption measurement was performed three times, so that the hydrogen capacity was calculated as an average. Measurements of the hydrogen desorption rate were performed through a mass flow controller. These measurements only give an estimation of the time required for the hydrogen desorption, since the Mg–Fe–H systems under study release more hydrogen than the flow mass controller can intake.

3. Results and discussion

3.1. Preparation of Mg–Fe–H hydride systems by reactive ball milling

Mg–Fe–H hydride systems were synthesized via RBM in hydrogen atmosphere using as initial materials Mg_xFe (x: 2, 3 and 15); the details of the milling processes can be seen in Table 1. In Fig. 1 are presented the XRD diffraction patterns at 30 h and 150–200 h

Table 1
Processing parameters for the reactive mechanical milling carried out with different Mg–Fe stoichiometric mixtures.

Sample	Atmosphere[a]	Ball to powder ratio	Milling ode	Vial speed [rpm]	Temperature [K]	Final milling time [h]
Mg_2Fe[b]	H_2 (0.5 MPa)	~44:1	Low energy	~180	~300	200
Mg_3Fe[c]	H_2 (0.5 MPa)	~47:1	Low energy	~180	~300	150
$Mg_{15}Fe$[c]	H_2 (0.5 MPa)	~44:1	Low energy	~180	~300	150

[a] Hydrogen purity: +99.999%.
[b] Mg powder with an agglomerate size distribution between 130 and 260 μm and Fe powder with an agglomerate size distribution between 40 and 130 μm (estimated by particle size distribution analysis—Mastersizer Micro. MAF 5000).
[c] Mg and Fe powders with an agglomerate size >1000 μm.

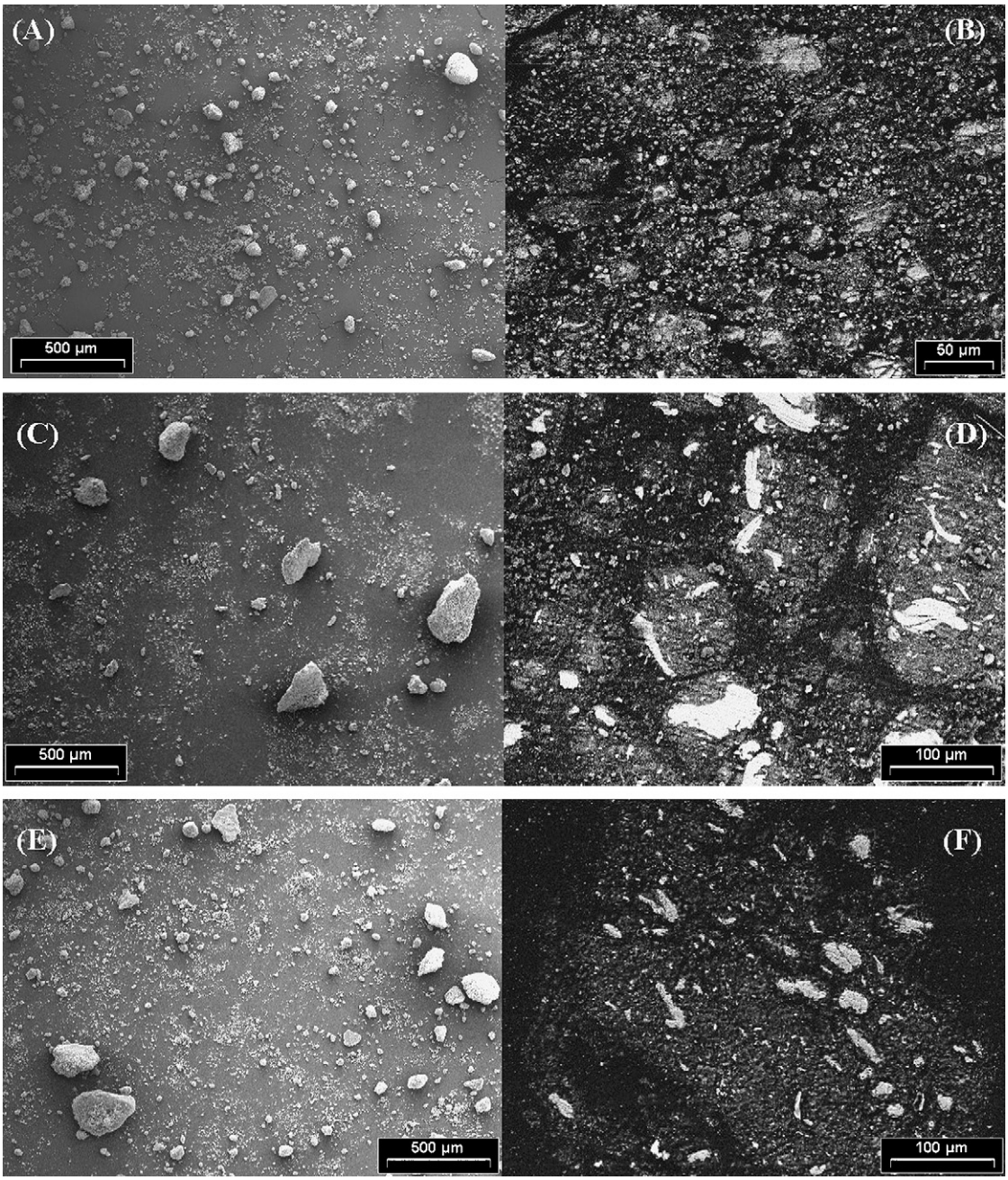

Fig. 2. Secondary electron micrographs showing the conglomerate size distribution (on the left) and backscattered electrons micrographs showing the dispersion of Fe (bright phase) and Mg (dark phase) of the as-milled powders (on the right). (A) and (B) Mg_2Fe after 200 h of RBM, (C) and (D) Mg_3Fe after 150 h of RBM and (E) and (F) $Mg_{15}Fe$ after 150 h of RBM.

of RBM. At 30 h of RBM, in all the investigated compositions β-MgH_2 (JCPDS Powder Diffraction Data Card No. 12–0697), Fe (JCPDS Powder Diffraction Data Card No. 06–0696) and Mg (JCPDS Powder Diffraction Data Card No. 35–0821) phases were identified. The XRD patterns taken between 30 h and the final milling time are not shown as the unique hydride phase detected was β-MgH_2. In the case of the Mg_2Fe composition, at 200 h of RBM two small peaks of the intermetallic hydride Mg_2FeH_6 (JCPDS Powder Diffraction Data Card No. 38–0843) appeared, coexisting with β-MgH_2 and unreacted Fe. Considering the reported information about the synthesis of Mg_2FeH_6 via low energy RBM from 2Mg–Fe, the fact that the ternary complex was formed after long hours of milling is attributed to the insufficient energy input due to the low energy milling mode, insufficient nanostructurization of Fe and the insufficient nanocrystalline β-MgH_2 required to react with Fe [34–37]. Moreover, the low intensity of the Mg_2FeH_6 peaks is attributed to the high amorphisation degree reached after 200 h of RBM.

After milling, in the XRD pattern of Mg_3Fe (Fig. 1) only β-MgH_2 and unreacted Fe were detected. In the case of as-milled $Mg_{15}Fe$, β-MgH_2 and Fe were also present together with the metastable γ-MgH_2 (JCPDS Powder Diffraction Data Card No. 35–1184) and MgO (JCPDS Powder Diffraction Data Card No. 45–0946). Metastable γ-MgH_2 appeared owing to the structural defects and the mechanical deformation that occur during the RBM [6]. The presence of MgO only in $Mg_{15}Fe$ composition can be attributed to a larger surface area of free Mg generated by the milling process, large proportion of Mg particles which are not coated with Fe and the high reactivity of Mg to oxygen.

An estimation of the crystallite size reduction was carried out by Scherrer equation. For Mg_2Fe, Mg_3Fe and $Mg_{15}Fe$, the crystallite size of MgH_2 (lattice plane (1 1 0), 2θ: 27.9°) and Fe (lattice plane (1 1 1), 2θ: 44.5°) reached stable values after 100 h of RBM (XRD not shown). Taking into account the crystallite size of the initial materials (Mg_2Fe: Fe ~40 nm and Mg ~50 nm; Mg_3Fe and $Mg_{15}Fe$: Fe and Mg >1000 nm) and the peak broadening observed in all XRD patterns of the samples (Fig. 1), it is clear that the crystallite size has been reduced as a direct consequence of the RBM process. The final crystallite size values of MgH_2 and Fe are in the order of ~10 nm and ~30 nm respectively.

Fig. 2 shows secondary electrons (on the left) and backscattered electrons (on the right) images of the as-milled powders. The agglomerate size distributions are between 10 and 150 μm for Mg_2Fe (Fig. 2A) and 10 and 300 μm for Mg_3Fe and $Mg_{15}Fe$ compositions (Fig. 2C and E). The conglomerate average sizes of the as-milled powders range between 20 and 30 μm and present a spherical porous kind morphology. This evidences that the conglomerates size of the materials has been reduced in comparison to the initial materials (see Table 1). Micrographs taken on resin-mounted and polished powders show the intermixture degree between Mg and Fe. For Mg_2Fe composition, the iron particles embedded in the Mg matrix cannot be distinguished showing a good intermixing degree and particle size reduction (Fig. 2B). On the other hand, particles of Fe bigger than 50 μm can be observed in the micrographs of Mg_3Fe and $Mg_{15}Fe$ compositions (Fig. 2D and F). Hence, the intermixture degree and particle size reduction reached in Mg_3Fe and $Mg_{15}Fe$ is not as effective as in Mg_2Fe. Considering the same milling conditions, this fact can be attributed to the smaller conglomerate size of the initial materials (see Table 1) and the further refinement degree rendered by larger amounts of Fe [9].

The reduction of the crystallite and agglomerate size is caused by the mechanical action of the grinding medium, the embrittlement of Mg by hydrogen gas and the in situ formation of MgH_2 brittle phase [34]. While the crystallite size reduction down to the nanometer range enhances the hydrogen transport properties of the hydride materials, the reduction of the agglomerate size results in an increase of specific area for hydrogen absorption. Both effects improve the kinetic characteristics of the Mg–Fe based materials [9,10,23,25].

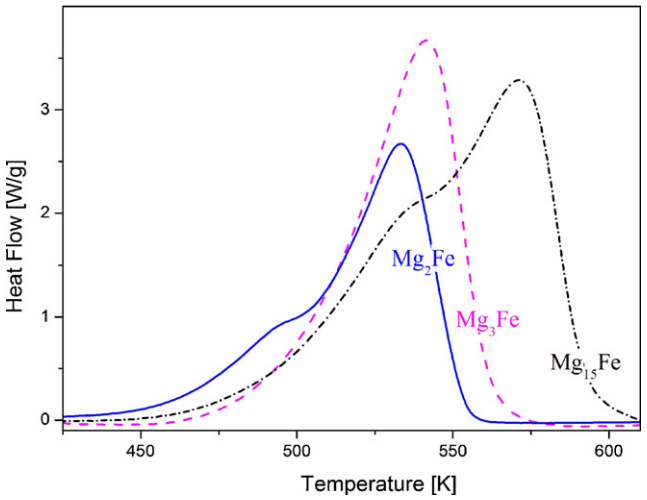

Fig. 3. Hydrogen desorption from the as-milled Mg_2Fe, Mg_3Fe and $Mg_{15}Fe$ compositions.

In Fig. 3 are shown the DSC curves of the synthesized MgH_2–Fe compositions. From these curves the maximum desorption temperatures are subtracted and the relative amount of hydride phases and hydrogen capacity estimated (with an error of ±5%). The amounts of unreacted Mg and Fe are calculated taking into account the percentages of hydride phases and the stoichiometric proportions of the initial materials, see Table 2. The initial desorption temperature is about 475 K and it does not change with the quantity of Fe, from 7 to 39 wt%. Moreover, as proportion of Fe increases the total hydrogen capacity decreases from 6.9 to 4.1 wt% H.

The non-symmetrical shape of the DSC curve of Mg_2Fe can be assigned to the presence of Mg_2FeH_6 identified in the XRD pattern, see Fig. 1 (Section 3.1), as Mg_2FeH_6 decomposes at lower temperatures than MgH_2 [37]. The deconvolution of the DSC curve of the as-milled powders gives an estimation of the relative amounts of MgH_2 and Mg_2FeH_6, see Table 2. It is considered that the amount of the ternary hydride obtained from DSC analysis does not contradict the low intensity peaks observed in the XRD pattern of Mg_2Fe (Fig. 1, Section 3.1) owing to the high degree of amorphisation of this hydride phase after long milling. The DSC curve of $Mg_{15}Fe$ also presents a non-symmetrical form. This is due to the lower decomposition temperature of the metastable γ-MgH_2 [6].

The desorption temperatures of the milled materials are substantially lower than that of the non-milled MgH_2, ~720 K [16]. This reduction is a consequence of two factors. First, the microstructural changes induced by milling, i.e. particle size reduction, crystallite size reduction, creation of grain boundaries and defects density [34,38]. Second, the catalytic effect produced by Fe [34,36,38], since the desorption temperature of milled MgH_2 (milled for 100 h,

Table 2
Estimation of the relative amount of phases (±5% error) of the as-milled compositions and maximum desorption temperature from DSC analysis.

Sample	Tpeak [K]	Relative amount of phases [wt%]				Total hydrogen amount [wt%]
		MgH_2	Mg_2FeH_6	Mg	Fe	
Mg_2Fe	533	36	25	2	37	4.1
Mg_3Fe	541	60	–	1	39	4.6
$Mg_{15}Fe$	571	90	–	3	7	6.9

Table 3
Equilibrium pressures and relative amount of hydrogen stored in the Mg–Fe–H hydride system as a function of the temperature, obtained from the absorption/desorption PCI curves.

Sample	Temperature [K]	Absorption		Desorption			
		MgH_2–Mg_2FeH_6		MgH_2		Mg_2FeH_6	
		P_{eq} [kPa]	Hydrogen content [wt%]	P_{eq} [kPa]	Hydrogen content [wt%]	P_{eq} [kPa]	Hydrogen content [wt%]
Mg_2Fe	673	1925 ± 100	3.90	1565 ± 30	0.93	900 ± 60	2.97
	648	1160 ± 70	2.80	1000 ± 40	0.90	470 ± 130	1.90
	623	730 ± 20	2.60	590 ± 20	1.95	260 ± 65	0.65
	573	250 ± 30	2.00	163 ± 11	2.00	–	–
	523	60 ± 4	1.90	50 ± 1	1.58	–	–
Mg_3Fe	673	2360 ± 160	4.20	1955 ± 45	2.80	915 ± 40	0.90
	648	1440 ± 80	4.00	1210 ± 40	3.42	510 ± 70	0.53
	623	865 ± 65	3.90	710 ± 30	3.80	–	–
	573	290 ± 60	3.70	200 ± 10	3.70	–	–
	523	75 ± 30	2.80	40 ± 4	2.80	–	–
$Mg_{15}Fe$	673	1955 ± 43	6.15	1700 ± 57	5.95	900 ± 40	0.20
	663	1600 ± 35	6.05	1380 ± 40	5.95	650 ± 60	0.10
	648	1245 ± 80	6.00	1010 ± 37	6.00	510 ± 90	0.05
	633	980 ± 80	6.00	750 ± 24	6.00	–	–
	623	800 ± 88	6.00	580 ± 30	6.00	–	–
	573	190 ± 8	5.50	170 ± 7	5.50	–	–
	548	150 ± 48	5.30	88 ± 6	5.30	–	–
	523	70 ± 24	3.90	47 ± 3	3.90	–	–

crystallite size of 12 nm) is 655 K [39,40]. As it can be noticed, the decomposition temperature lowers as the Fe proportion is increased. However, a small quantity of Fe is enough to reduce the decomposition temperature and to reach better hydrogen capacity.

The reactive ball milling method has been used to synthesized hydride materials from Mg_xFe (x: 2, 3 and 15). Via this one step synthesis procedure nanostructurized materials composed by different amounts of hydride phases have been obtained. Among the investigated compositions, $Mg_{15}Fe$ has the higher yield of hydride phase and hydrogen capacity, see Table 2.

3.2. Thermodynamic characterization

The equilibrium properties of the synthesized Mg–Fe–H systems were examined between 523 and 673 K. Pressure–composition isotherms were measured to determine the absorption/desorption equilibrium pressures and hydrogen capacities of the Mg_2Fe, Mg_3Fe and $Mg_{15}Fe$ compositions. The equilibrium pressures and hydrogen reversible capacities were estimated from the plateau widths. As it can be noticed in Table 3 as well as in Fig. 4, hydrogen capacities and equilibrium pressures decrease as the temperature falls. This is due to the atom diffusion mechanisms which are hampered by the lower temperatures [41].

The PCI of the extreme compositions, viz. Mg_2Fe and $Mg_{15}Fe$, can be observed in Fig. 4. The hydrogen absorption/desorption stoichiometric reactions can be seen in Ref. [42]. One plateau is only observed during the absorption processes because the equilibrium pressures of Mg_2FeH_6 and MgH_2 are similar [41]. On the other hand the equilibrium pressures of MgH_2 and Mg_2FeH_6 during the release of hydrogen are different, thus hydrogen desorption processes show two plateaus. In the case of Mg_2Fe, two plateaus can be noticed during the desorption process at temperatures above 623 K. This is a result of the Mg_2FeH_6 formation via thermal enhanced atom diffusion mechanism during the hydrogen absorption. For Mg_3Fe and $Mg_{15}Fe$, two desorption plateaus are observed at temperatures above 648 K, but they are not seen at 623 K. In this case, the amount of available Fe is not in the right stoichiometric proportion for the Mg_2FeH_6 formation, the Fe conglomerates are in

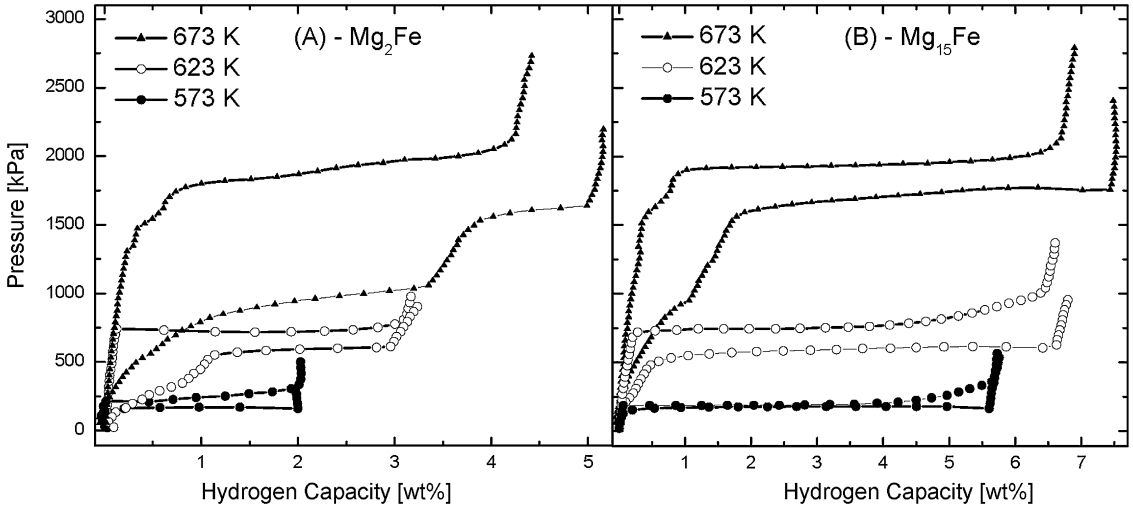

Fig. 4. Pressure–composition isotherms for (A) Mg_2Fe and (B) $Mg_{15}Fe$ compositions at 573, 623 and 673 K.

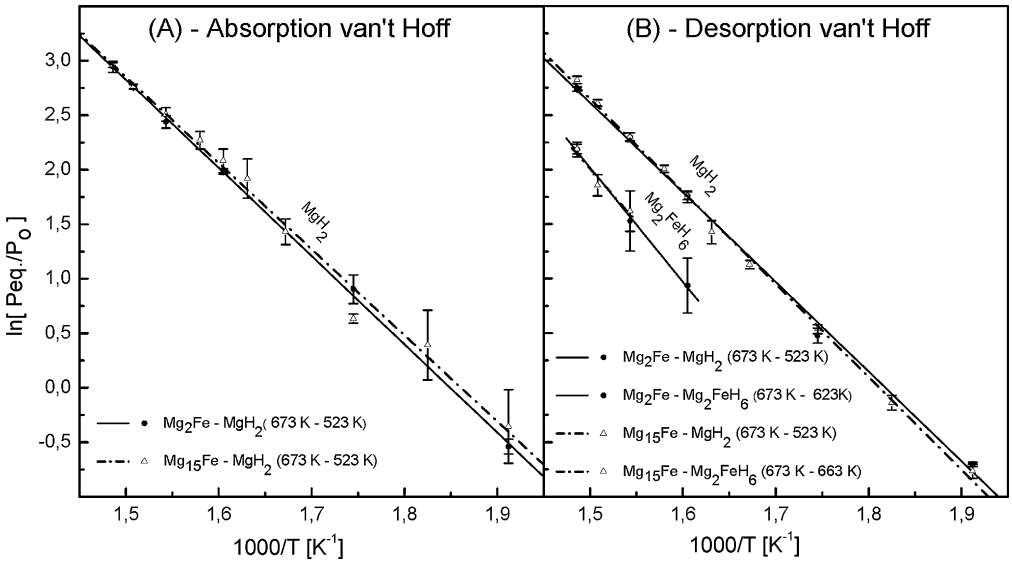

Fig. 5. (A) Absorption and (B) desorption van't Hoff plots of the (— fitting, △ experimental) Mg_2Fe and (– · – fitting, ● experimental) $Mg_{15}Fe$ compositions.

the order of 50 μm and are not well dispersed as in Mg_2Fe composition (see Fig. 2—backscattered electrons). Therefore, below 648 K the thermal enhanced atom diffusion mechanism to form Mg_2FeH_6 during the hydrogen absorption process might be hampered by the poor Fe–Mg contacting. The presence of one absorption/desorption plateau below 623 K (Mg_2Fe) and 648 K (Mg_3Fe and $Mg_{15}Fe$) is attributed to MgH_2 which is the unique hydride phase formed during the hydrogen absorption process [40].

Another important characteristic shown in Fig. 4 is the phenomenon of hysteresis in the absorption/desorption cycles. As the temperature increases it becomes more noticeable. It can be clearly observed in the PCIs of the Mg_2Fe composition, even at 573 K. On the contrast, it is not too pronounced in the PCI cycles of the $Mg_{15}Fe$ composition. The phenomenon of hysteresis is ascribed to elastic and plastic strain energies related to the volume changes during the formation of the hydride phases [43]. Moreover, at temperatures above 623 K, at which Mg_2FeH_6 is formed during the hydrogen absorption process, the hysteresis arises manly from the presence of Mg_2FeH_6 [44,45].

The thermodynamic parameters (absorption/desorption enthalpy and entropy) of Mg_2Fe, Mg_3Fe and $Mg_{15}Fe$ compositions were calculated from the van't Hoff graphs. In Fig. 5 are shown the absorption/desorption van't Hoff plots of the extreme compositions, i.e. Mg_2Fe and $Mg_{15}Fe$, in the temperature range of 523–673 K. For the sake of clarity and due to the similarity of the calculated thermodynamic parameters of Mg_3Fe (Table 4), the van't Hoff plots of this intermediate composition are not included in Fig. 5.

In Table 4 the values of enthalpy and entropy are shown and compared with those found in the literature and our previous works [32,40–42,46–48]. The calculated parameters show a good correlation with those found in the literature for the hydride mixture. The differences between the values of calculated parameters and those reported in the literature might be related to the measurement procedure and the temperature ranges considered.

The assessed compositions, i.e. Mg_2Fe, Mg_3Fe and $Mg_{15}Fe$, present thermodynamic parameters that lay in the same range. This shows that the thermodynamic of the Mg–Fe–H system is not mod-

Table 4
Formation and decomposition enthalpies and entropies obtained from the van't Hoff plot of the Mg–Fe–H hydride system synthesized from different stoichiometric compositions.

Absorption	MgH_2 and Mg_2FeH_6	
	ΔH [kJ mol^{-1} H_2]	ΔS [J mol^{-1} H_2 K^{-1}]
Mg_2Fe (523–673 K)	−68 ± 1	−124 ± 2
Mg_3Fe (523–673 K)	−68 ± 5	−127 ± 7
$Mg_{15}Fe$ (523–673 K)	−65 ± 2	−122 ± 4
Ref. [41] (548–723 K)	−66 ± 2	−124 ± 3
Ref. [48] (698–723 K)	−55 ± 3	–

Desorption	MgH_2		Mg_2FeH_6	
	ΔH [kJ mol^{-1} H_2]	ΔS [J mol^{-1} H_2 K^{-1}]	ΔH [kJ mol^{-1} H_2]	ΔS [J mol^{-1} H_2 K^{-1}]
Mg_2Fe (523–673 K)	−68 ± 2	−124 ± 3	−87 ± 5	−147 ± 7
Mg_3Fe (523–673 K)	−76 ± 1	−138 ± 2	−85	−144
$Mg_{15}Fe$ (523–673 K)	−71 ± 1	−128 ± 2	−96 ± 24	−161 ± 36
Ref. [41] (548–648 K)[1], (573–648 K)[2]	−67 ± 2[1]	−123 ± 3[1]	−80 ± 7[2]	−137 ± 13[2]
Ref. [42] (573–673 K)	−79 ± 3	−140 ± 7	−87 ± 3	−147 ± 15
Ref. [46] (587–849 K)	−74	135	–	–
Ref. [47] (648–723 K)	–	–	−98 ± 3	–
Ref. [48] (623–698 K)	−77 ± 4	−138 ± 3	−86 ± 6	−147 ± 9
Ref. [32] (623–798 K)	–	–	−77	–

Table 5
Hydrogen absorbed in 500 s at 523, 573, 623 and 673 K after a number of hydrogen absorption/desorption cycles, between parentheses.

Sample	Theoretical capacity H [wt%]	H [wt%] absorbed in 500 s at different temperatures			
		523 K	573 K	623 K	673 K
Mg_2Fe	3.8	0.95 (80)	1.35 (100)	1.70 (110)	2.50 (120)
Mg_3Fe	4.7	1.40 (10)	2.4 (20)	3.45 (35)	3.50 (50)
$Mg_{15}Fe$	7.1	1.50 (50)	3.00 (60)	4.85 (110)	4.90 (100)

Table 6
Integral forms of various gas–solid kinetics models used for fitting experimental sorption data [49,50].

Model	Description	Integral form $g(\alpha)=k\cdot t$
Nucleation models		
Johnson–Mehl–Avrami (JAM), $n=2$	Two-dimensional growth of existing nuclei with constant interface velocity.	$[\ln(1-\alpha)]^{1/n}$
Johnson–Mehl–Avrami (JAM), $n=3$	Three-dimensional growth of existing nuclei with constant interface velocity.	
Geometrical contracting models		
Contracting area (CA)	Two-dimensional growth with phase boundary controlled reaction.	$1-(1-\alpha)^{1/2}$
Contracting volume (CV)	Three-dimensional growth with phase boundary controlled reaction.	$1-(1-\alpha)^{1/3}$
Diffusion models		
1D diffusion	Surface controlled (chemisorption).	α^2
2D diffusion	Two-dimensional growth diffusion controlled with decreasing interface velocity.	$[(1-\alpha)\ln(1-\alpha)]+\alpha$
3D diffusion (Ginstling–Brounshtein)	Three-dimensional growth diffusion controlled with decreasing interface velocity.	$1-(2/3)\alpha-(1-\alpha)^{2/3}$

ified by the stoichiometric proportions of Mg and Fe. It is also worth noting that $Mg_{15}Fe$ has the advantages of higher capacity than the other compositions and small hysteresis between the hydrogen uptake and release. These two features are quite important for potential practical applications.

3.3. Kinetics: hydrogen realize/uptake behavior

The kinetic behavior was investigated between 523 and 673 K using an established relationship of $P/P_{equilibrium}$ equal to 2.4 in a Sieverts-type device. Measurements of the hydrogen absorption capacity reached in 500 s and after different numbers of absorption/desorption cycles are shown in Table 5. The reported capacities correspond to MgH_2 in presence of free Fe. At an intermediate temperature, 623 K, the hydride material composed by $Mg_{15}Fe$ shows a capacity of 4.85 wt% H absorbed in less than 10 min and after 100 absorption/desorption cycles. These hydrogen storage uptake characteristics are better in comparison to the other compositions and are also interesting conditions for a potential application.

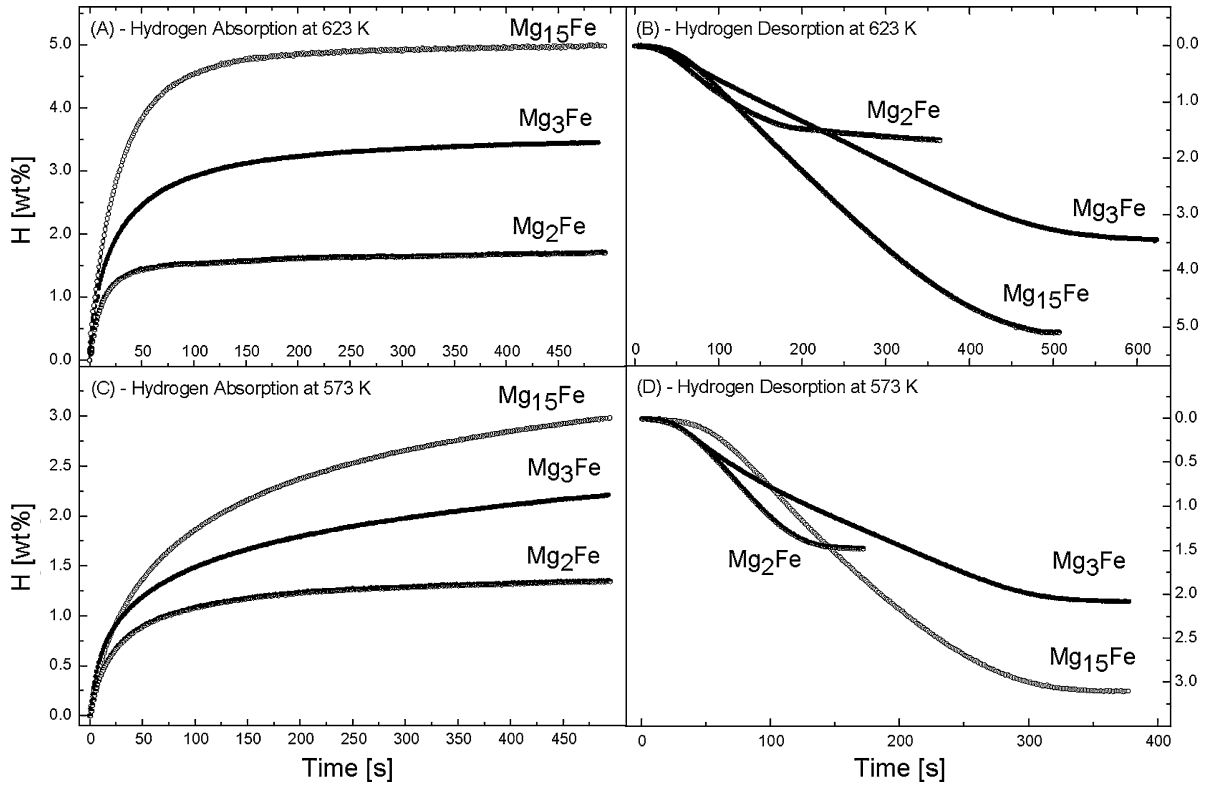

Fig. 6. Hydrogen absorption/desorption rate for the different Mg–Fe compositions: (A) absorption kinetics and (B) desorption kinetics at 623 K; (C) absorption kinetics and (D) desorption kinetics at 573 K.

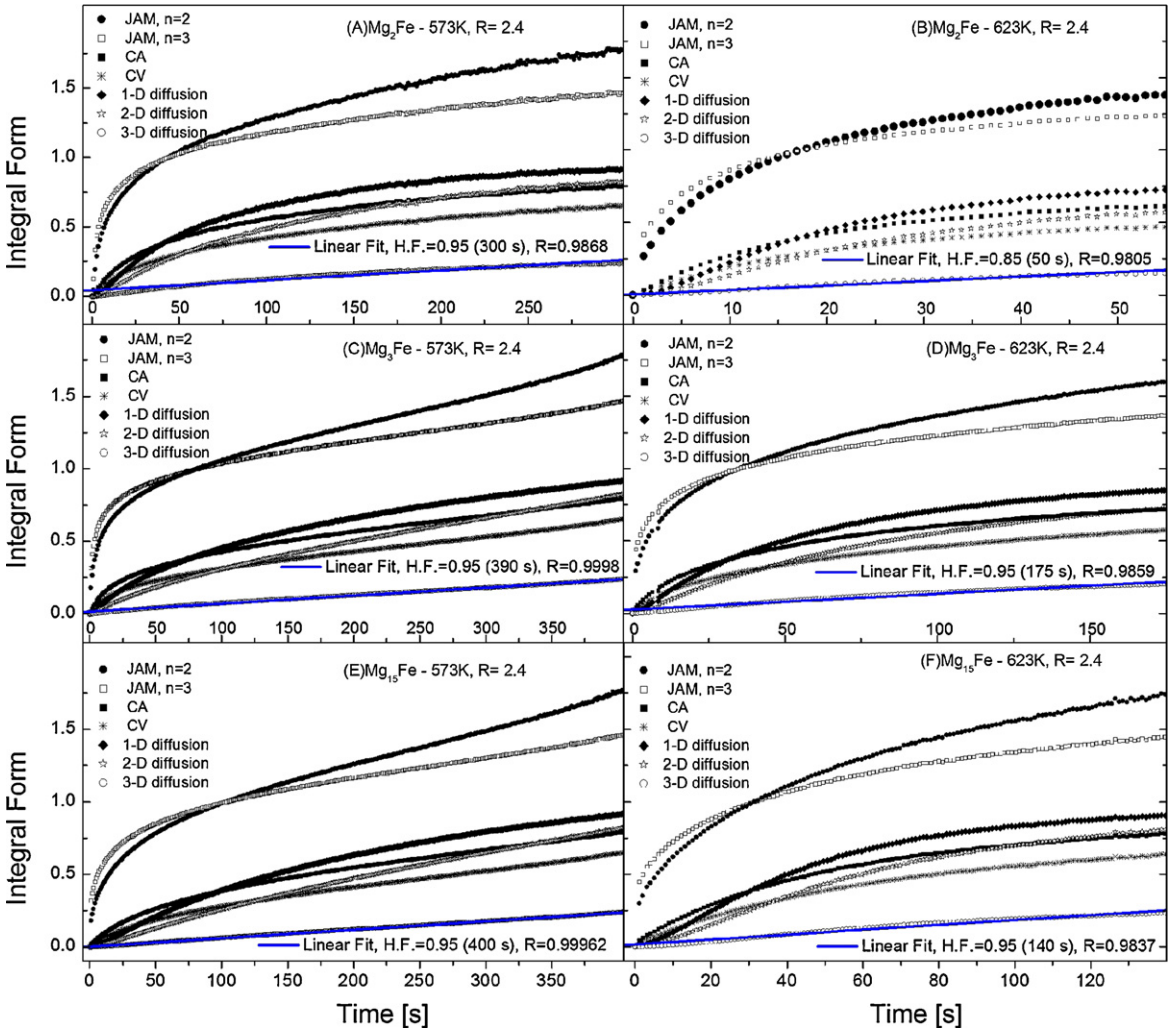

Fig. 7. Curves resulted from the application of the integral forms of the particle kinetics models to the hydrogen absorption rate measurements at 573 and 623 K for the different Mg–Fe compositions (Fig. 6). — Linear fits; the absorbed hydrogen fraction, H.F., followed by the range of time required to reach the specified H.F. (between parentheses) and the correlation coefficient, *R*, are indicated.

A comparison between the hydrogen absorption and desorption rates at 523 and 623 K is shown in Fig. 6. At 623 K (Fig. 6A), it is clear that $Mg_{15}Fe$ is faster than the other compositions. However, at 573 K (Fig. 6C), the rate of hydrogen uptake of Mg_3Fe is slightly faster than $Mg_{15}Fe$. The hydrogen release behavior of the hydride materials is shown in Fig. 6B and D. Due to the experimental limitations (see Section 2.2), these measurements are an estimation of the times required for the hydrogen desorption. At 573 and 623 K, desorption times range between 400 and 600 s. In the case of $Mg_{15}Fe$, which is the composition with higher capacity, at 573 and 623 K the hydrogen release takes 400 and 500 s respectively.

In order to obtain information about the reaction mechanism during the hydrogen uptake, an analysis of the curves shown in Fig. 6A and C applying gas–solid kinetic models was performed. The general expression to study the rate of gas–solid reactions is as follows

$$\frac{d\alpha}{dt} = K(T) \times F(P) \times G(\alpha) \quad (1)$$

where the overall reaction rate is function of the temperature (T), hydrogen gas pressure (P) and the absorbed hydrogen fraction (α—defined in this work as fraction of the total hydrogen wt% reached in 500 s). The temperature term is a function of the Arrhenius equation $K(T) = A \times e^{-(Ea/RT)}$, and the $F(P)$ term is taken as $P/P_{equilibrium}$ equal to 2.4. Considering that $K(T)$ does not change at given temperature and $F(P)$ is constant, Eq. (1) can be expressed as

$$g(\alpha) = \int_0^{\alpha} \frac{d\alpha}{G(\alpha)} = k \times t \quad (2)$$

where $g(\alpha)$ is the integral form of the models, which are shown in Table 6.

Although metal–hydrogen reactions involve a complex sequence of steps, in the above context a simplified scheme with three steps can be proposed. In this sense, hydriding reaction involves a first stage starting at the gas-surface region, following by the nucleation/growth of the hydride phase and ending with the diffusion through the transformed phase. When absorption rate is governed by one of these steps, the kinetic rate-limiting step can be identified by fitting the integral equations of the particle reaction models (Table 6).

The reaction of Mg and Mg-based materials with hydrogen is influenced by three dominant factors: crystallite size, particle size and catalyst [50]. From the application of the integral forms of various gas–solid kinetics models (Table 1) to the absorbed hydrogen fraction, α, reached in 500 s (Fig. 7), it is evident that the mechanism is neither surface controlled nor nucleation/growth controlled. This behavior is attributed to the catalytic effect of Fe on the hydro-

gen dissociation and the refinement degree of the microstructure, respectively. As it can be observed, for all the practised compositions the best fit is obtained with the 3D diffusion model, which indicates that the hydrogen mechanism is controlled by the diffusion of hydrogen into the MgH_2 bulk. Our results are in agreement with the previously reported for hydrogen absorption in milled MgH_2 catalyzed with Nb_2O_3 [50]. Then, the microstructural refinement and the dispersion of Fe imparted by RBM have enhanced both hydrogen dissociation and nucleation/growth rate, without effect on the hydrogen diffusion coefficient through the hydride phase.

4. Conclusion

Mg–Fe based materials for hydrogen storage were produced via RBM using mixtures of Mg_xFe (x: 2, 3 and 15) elemental powders. Via this one step method of synthesis, a high degree of microstructural refinement and catalyst dispersion (Fe), which enhanced the hydrogen storage properties, was reached. The higher yield of hydride phase (90 wt% of MgH_2) and hydrogen capacity (6.9 wt% H) was obtained from the $Mg_{15}Fe$ composition. Studies under equilibrium conditions showed that the thermodynamic parameters for different Mg–Fe compositions are similar and are in good agreement with those reported in the literature. An assessment of the hydrogen uptake reaction mechanism by fitting kinetic models showed that the absorption reaction is diffusion controlled. This mechanism does not change with the Mg–Fe proportion at the measured temperatures.

From the studied compositions, $Mg_{15}Fe$ showed the highest hydrogen capacity (4.85 wt% H after 100 absorption/desorption cycles at 623 K), reasonable absorption/desorption times (absorbs 90% of its final capacity in about 200 s and the hydrogen release takes 600 s) and narrow hysteresis cycle. These are promising characteristics from the application point of view.

Acknowledgments

The authors thank CONICET, ANPCyT and Institut Balseiro (UNCuyo) for financial support to carry out this work.

References

[1] S. Satyapal, J. Petrovic, C. Read, G. Thomas, G. Ordaz, Catal. Today 120 (2007) 246–256.
[2] R.C. Weast, M.J. Astle, W.H. Beyer, Handbook of Chemistry and Physics, 60th ed., The Chemical Rubber Co., Boca Raton, 1979.
[3] W. Grochala, P. Edwards, Chem. Rev. 104 (2004) 1283–1316.
[4] A. Zaluska, L. Zaluski, J.O. Ström-Olsen, J. Alloys Compd. 288 (1999) 217–225.
[5] J. Huot, G. Liang, S. Boily, A. Van Neste, R. Schulz, J. Alloys Compd. 293–295 (1999) 495.
[6] F.C. Gennari, F.J. Castro, G. Urretavizcaya, J. Alloys Compd. 321 (2001) 46–53.
[7] J. Huot, M.L. Tremblay, R. Schulz, J. Alloys Compd. 356/357 (2003) 603–607.
[8] J.L. Bobet, S. Desmoulins-Krawiec, E. Grigorova, R. Cansell, B. Chevalier, J. Alloys Compd. 351 (2003) 217–221.
[9] A. Bassetti, E. Bonetti, L. Pasquini, A. Montone, J. Grbovic, M. Vittori, Antisari, Eur. Phys. J. B 43 (2005).
[10] G. Liang, J. Huot, S. Boily, A.V. Neste, R. Schulz, J. Alloys Compd. 291 (1999) 295–299.
[11] G. Liang, J. Huot, S. Boily, R. Schulz, J. Alloys Compd. 305 (2000) 239.
[12] S.R. Ovshinsky, M.A. Fetcenko, Appl. Phys. A 72 (2001) 239.
[13] J. Huot, J.F. Pelletier, L.B. Lurio, M. sutton, R. Schulz, J. Alloys Compd. 248 (2003) 319.
[14] A. Zaluska, L. Zaluski, J.O. Ström-Olsen, J. Alloys Compd. 289 (1999) 197–206.
[15] G. Liang, J. Huot, S. Boily, A.V. Neste, R. Schulz, J. Alloys Compd. 292 (1999) 247–252.
[16] H. Reule, M. Hirscher, A. Weißhardt, H. Kronmuller, J. Alloys Compd. 305 (2000) 246–252.
[17] Z. Dehouche, J. Goyette, T.K. Bose, J. Huot, R. Schulz, Nano Lett. 1 (2001) 175–178.
[18] W. Oelerich, T. Klassen, R. Bormann, J. Alloys Compd. 315 (2001) 237–242.
[19] J.F. Pelletier, J. Huot, M. Sutton, R. Schulz, A.R. Sandy, L.B. Lurio, S.G.J. Mochrie, Phys. Rev. B 63 (2001) 052103.
[20] G. Barkhordarian, T. Klassen, R. Bormann, Scripta Mater. 49 (2003) 213–217.
[21] G. Liang, J. Alloys Compd. 370 (2004) 123–128.
[22] J.F.R. De Castro, S.F. Santos, A.L.M. Costa, A.R. Yavari, W.J. Botta, T.T. Ishikawa, J. Alloys Compd. 376 (2004) 251–256.
[23] J. Charbonnier, P. de Rango, D. Fruchart, S. Miraglia, L. Pontonnier, S. Rivoirard, N. Skryabina, P. Vulliet, J. Alloys Compd. 383 (2004) 205–208.
[24] J.J. Vajo, F. Mertens, C.C. Ahn, R.C. Bowman Jr., B. Fultz, J. Phys. Chem. B 108 (2004) 13977–13983.
[25] N. Hanada, T. Ichikawa, H. Fujii, J. Phys. Chem. B 109 (2005) 7188–7194.
[26] M.-Y. Song, D.R. Mumm, S.-N. Kwon, S.-H. Hong, J.-S. Bae, J. Alloys Compd. 416 (2006) 239–244.
[27] G. Barkhordarian, T. Klassen, R. Bormann, J. Phys. Chem. B 110 (2006) 11020–11024.
[28] X. Yao, C. Wu, A. Du, G.Q. Lu, H. Cheng, S.C. Smith, J. Zou, Y. He, J. Phys. Chem. B 110 (2006) 11697–11703.
[29] V.V. Bhat, A. Rougier, L. Aymard, X. Darok, G. Nazri, J.M. Tarascon, J. Power Sources 159 (2006) 107–110.
[30] S.-A. Jin, J.-H. Shim, Y.W. Cho, K.-W. Yi, J. Power Sources 172 (2007) 859–862.
[31] Y.J. Choi, J. Lu, H.Y. Sohn, Z.Z. Fang, J. Power Sources 180 (2008) 491–497.
[32] B. Bogdanović, A. Reiser, K. Schlichte, B. Spliethoff, B. Tesche, J. Alloys Compd. 345 (2002) 77–89.
[33] G. Meyer, D.S. Rodríguez, F. Castro, G. Fernández, Hydrogen Energy Progress, Proceedings of the 11th World energy Conference, Stuttgart, Germany, June 23–29, 1996, pp. 1293–1298.
[34] F.C. Gennari, F.J. Castro, J.J. Andrade Gamboa, J. Alloys Compd. 339 (2002) 261–267.
[35] R.A. Soglin Li, O. Varin, T. Morozoba, Khomenko, J. Alloys Compd. 384 (2004) 231–248.
[36] R.A. Varin, S. Li, Z. Wronski, O. Morozoba, T. Khomenko, J. Alloys Compd. 390 (2005) 282–296.
[37] F.J. Castro, F.C. Gennari, J. Alloys Compd. 375 (2004) 292–296.
[38] Y.G. Konstanchuk, E. Ivanov, M. Pezat, B. Darriet, V. Boldyrev, P. Hagenmuller, J. Less-Common Met. 131 (1987) 181–189.
[39] R.A. Varin, T. Czujko, E.B. Wasmund, Z.S. Wronski, J. Alloys Compd. 432 (2007) 217–231.
[40] J. Huot, H. Hayakawa, E. Akiba, J Alloys Compd. 248 (1997) 164–1677.
[41] J.A. Puszkiel, P. Arneodo Larochette, F.C. Gennari, J. Alloys Compd. 463 (2008) 134–142.
[42] J.A. Puszkiel, P. Arneodo Larochette, F.C. Gennari, Int. J. Hydrogen Energy 33 (2008) 3555–3560.
[43] P.S. Rudman, G. Sandrock, Annu. Rev. Mater. Sci. 12 (1982) 271–294.
[44] B. Bogdanovic˘, A. Reiser, K. Schlichte, B. Spliethoff, B. Tesche, J. Alloys Compd. 345 (2002) 77–89.
[45] J. Huot, S. Boily, E. Akiba, R. Schulz, J. Alloys Compd. 280 (1998) 306–309.
[46] J.F. Stampfer, C.E. Holley, J.F. Suttle, J. Am. Chem. Soc. 82–7 (1960) 3504–3508.
[47] J.-J. Didisheim, P. Zolliker, K. Yvon, P. Fisher, J. Schefer, M. Gubelmann, A.F. Williams, Inorg. Chem. 23 (1984) 1953–1957.
[48] P. Selvam, K. Yvon, Int. J. Hydrogen Energy 16 (9) (1991) 615–617.
[49] A. Khawam, D.R. Flanagan, J. Phys. Chem. B 110 (2006) 17315–17328.
[50] G. Barkhordarian, T. Klassen, R. Bormann, J. Alloys Compd. 407 (2006) 249–255.